







# Tectonic and seismic implications of an intersegment rupture

## The damaging May 11th 2011 Mw 5.2 Lorca, Spain, earthquake

José J. Martínez-Díaz , Marta Bejar-Pizarro , José A. Álvarez-Gómez , Flor de Lis Mancilla ,  
Daniel Stich , Gerardo Herrera , Jose Morales

---

### A B S T R A C T

On May 11th 2011, a Mw 5.2 earthquake stroke the city of Lorca in the SE Spain. This event caused 9 fatalities, 300 injuries and serious damage on the city and the surrounding areas. The Lorca earthquake occurred in the vicinity of a region bounding two well-known segments of a large active fault, the Alhama de Murcia fault (AMF). The Lorca earthquake offers a unique opportunity to study how strain is accommodated in an intersegment region of a large strike slip fault. We map recent tectonic structures in the epicentral region and we use radar interferometry to analyze the coseismic deformation. Combining these data with seismological observations of Lorca seismic sequence we first model the source of the earthquake. Then we analyze the influence of our preferred model in the adjacent segments by Coulomb failure stress modeling. The proposed earthquake source model suggests that this event ruptured an area of  $\sim 4 \times 3$  km within the complex structure that limits the Goñar-Lorca and Lorca-Totana segments of the AMF. The induced static stress change on the adjacent segments of the fault represents a seismic cycle advance equivalent to 200 to 1000 years of tectonic loading.

---

Betic Cordillera  
INSAR  
Coulomb stress transfer  
Seismic hazard  
Active tectonics  
Intersegment zone

### 1. Introduction

Active faults are organized in more or less uniform segments separated by intersegment regions, characterized either by a change in the geometry of the fault or by the presence of structural complexities (Elliott et al., 2012; Fliss et al., 2005; Harris and Day, 1993; King, 1986; Klinger, 2010; Shengji et al., 2011; Wesnousky, 2006). Segmentation is important because of its implications for the rupture behavior during earthquakes. Segments are fault slip prone areas during large earthquakes (DePolo et al., 1989; 1991), whereas intersegment zones are defined as areas where rupture begins or stops during an earthquake (e.g. Aochi et al., 2000; Jackson et al., 2006; Klinger et al., 2005; Lozos et al., 2011). This complex behavior is observed not only in the horizontal rupture propagation, but also in the rupture propagation at depth (Elliott et al., 2011; Jackson et al., 2006; Li et al., 2011; Nissen et al., 2010). During major and less frequent earthquakes, several segments can slip at a time, whereas the intersegment zones can behave as areas of high slip release. This occurred during the Wenchuan earthquake (Shen et al., 2009). In other cases these

zones behave as relaxation barriers and large ruptures skip over the intersegment area that remains unbroken (Das and Aki, 1977; Scholz, 1990). The study of small earthquakes that break these intersegment areas gives us the opportunity to analyze this complex behavior.

On May 11th 2011, a Mw 5.2 earthquake stroke the city of Lorca in south-eastern Spain. This earthquake occurred 2 h after a Mw 4.6 foreshock and caused 9 fatalities, 300 injuries, serious damage on 1164 buildings and economic losses over 1200 M€ (data from the Municipality of Lorca updated November 2011). The Lorca earthquake is especially significant because it occurred in the vicinity of a region bounding two well-known segments of a large active fault, the Alhama de Murcia fault (AMF) (Fig. 1). This fault is the source of Mw > 6.5 historical and pre-historical earthquakes (Martínez-Díaz et al., 2001). The AMF accommodates  $\sim 0.1$ – $0.6$  mm/year of the approximately 5 mm/year of convergence between African and Eurasian plates (Masana et al., 2004) and belongs to the Eastern Betics Shear Zone (Silva et al., 1993). The AMF is one of the largest faults of this shear zone. Most of the largest damaging historical earthquakes are related with this structure (Fig. 1). This fault presents a NE–SW direction; it is  $\sim 100$  km length and is divided into 4 segments: Goñar-Lorca; Lorca-Totana; Totana-Alhama de Murcia and Alhama de Murcia-Alcantarilla (Fig. 1B). Paleoseismic studies along

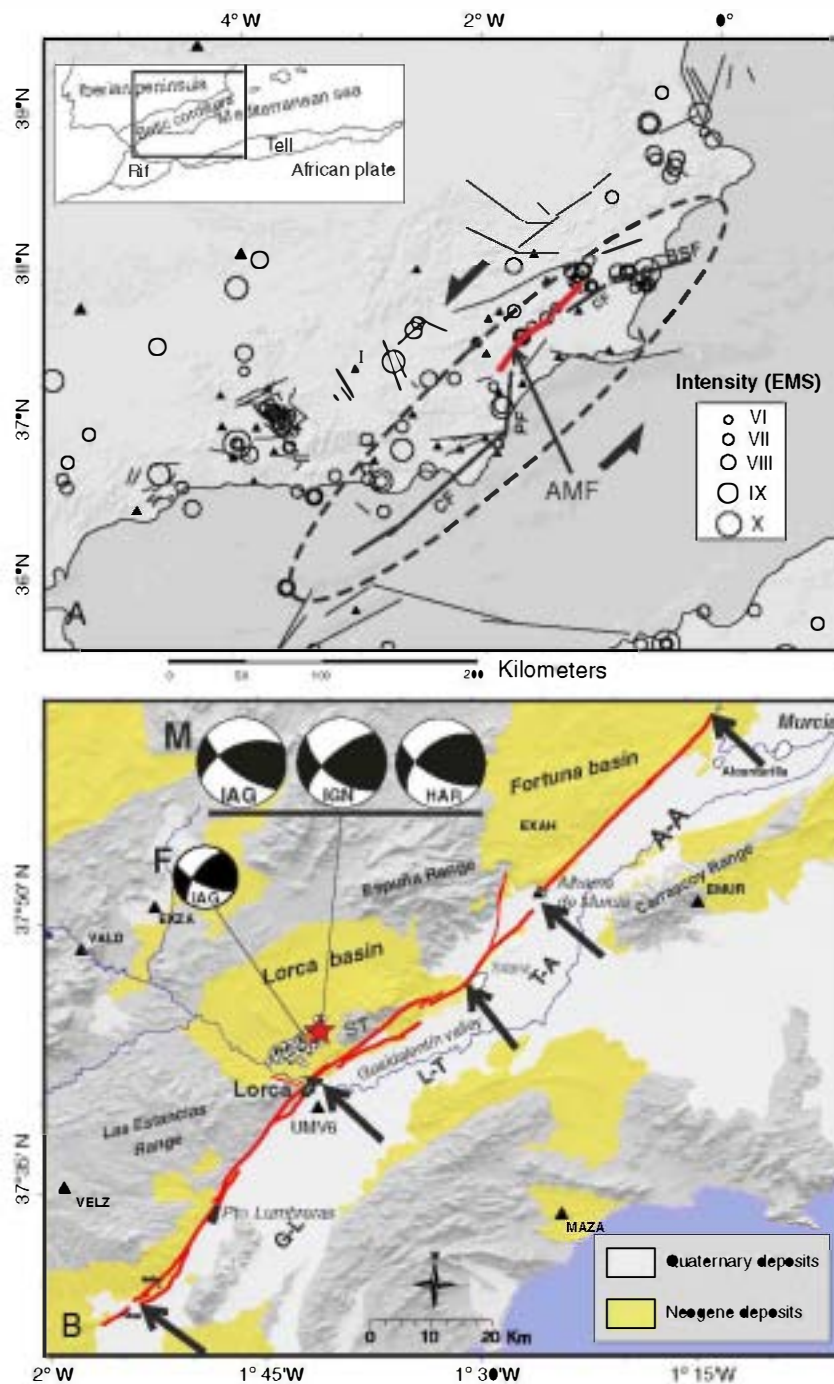


**Fig. 1.** A) Location map of the study area in which the Quaternary active faults are projected. Circles represent the historical seismicity with intensity (EMS) > VI (data from the Instituto Geográfico Nacional). The ellipse indicates the position of the Eastern Betic Shear Zone, CF: Carboneras fault; PF: Palomares fault; AMF: Alhama de Murcia fault; CCF: Carrascoy fault; BSF: Bajo Segura fault. B) Map of the Alhama de Murcia fault, arrows indicates the limits of the four main segments of this fault: GL: Goñar-Lorca segment, LT: Lorca-Totana Segment, TA: Totana-Alhama segment; AA: Alhama-Alcantarilla segment. ST: Sierra de La Tercia. The star and the circles are the mainshock and aftershocks of the Lorca 2011 seismic sequence taken from Lopez-Comino et al. (2012). Focal solutions of the foreshock (F) and the mainshock (M) from several agencies are shown, IAG: Instituto Andaluz de Geofísica; IGN: Instituto Geográfico Nacional; HARV: Harvard University. In both maps the black triangles are the seismic stations utilized in the aftershock relocation.

this fault suggest that the two segments converging on Lorca (Goñar-Lorca and Lorca-Totana) ruptured during the Quaternary as a single a seismogenic source producing earthquakes of  $M_w$  6.9–7.3 (Masana et al., 2005; Ortuño et al., 2012). Other paleoearthquakes identified on these segments are smaller ( $M_w$  ~6) and seem to have ruptured only one segment (Masana et al., 2004). The Lorca intersegment area could play a significant role in the seismogenic behavior of the AMF.

The Lorca earthquake offers a unique opportunity to study how strain is accommodated in this region that includes not only the AMF but also secondary active structures. We map recent tectonic structures in the epicentral region and we use radar interferometry to constrain the coseismic deformation. Combining these data with published seismological data of the seismic sequence of Lorca (Lopez-Comino et al., 2012) we model the earthquake source. Using Coulomb Failure Stress transfer ( $\Delta CFS$ ) models we analyze the



influence of our preferred source in the adjacent segments. We finally compare our results with topography and fault structure close to the rupture area and discuss the implications for strain accommodation, fault behavior and seismic hazards in the region.

## 2. Structure of the epicentral area

The Lorca 2011 earthquake occurred near the intersegment zone located between Goñar–Lorca and Lorca–Totana segments (Fig. 1). A field survey conducted in the epicentral area 2 days after the earthquake concluded that the Lorca earthquake did not rupture the surface (IGME, 2011). We performed detailed mapping of recent structures on the epicentral area to understand the kinematic of structures in the intersegment zone and to assess the potential source for the Lorca earthquake. For this purpose we use field data, aerial photography and a digital elevation model derived from LIDAR (Fig. 2). In this area the AMF undergoes a change of direction from N 55° to the northeast, to N 35° to the southwest. The structure of the fault is rather complex in this region, with a branched geometry due to the existence of contractional strike-slip duplex structures (Martínez-Díaz, 2002) and the interaction with the Las Viñas Fault to the north of Lorca. This is a WNW secondary fault that connects with the AMF generating a contracting slice raised by the movement of the AMF, which causes the lifting of the NE corner of the Sierra de Las Estancias (Fig. 2). Another example is the interaction between contemporary reverse, normal and strike-slip minor faults, and the disruption of the SW termination of the Sierra de La Tercia anticline.

The converging segments of the AMF in Lorca zone (GL and LT in Fig. 2) present a much simpler trace in the field and are observed dipping 55°–75° NW, and bounding the mountain fronts of the ranges. The reverse component of the movement produced this topography since upper Miocene (Martínez-Díaz, 2002). However, there is no relief in the intersegment zone where a depressed region dominates the morphology (Fig. 2).

Published focal mechanism for the Lorca 2011 earthquake present a nodal plane sub parallel to the AMF dipping to the north, being

the other nodal plane perpendicular to the AMF dipping to the SW (IAG, 2011; IGN, 2011) (Fig. 2). The latter is difficult to explain from the local structure. The former, on the other hand, is parallel to several branches of the AMF in the intersegment zone. Aftershocks registered until the 7th July were relocated by Lopez-Comino et al. (2012) using a dense seismic station network (Fig. 2). The aftershock epicenters aligned parallel to the AMF and concentrated on the north of the intersegment zone. These evidences suggest that the source of the earthquake is parallel to the AMF dipping to the north as proposed in a preliminary study by Vissers and Meijninger (2011). In this work we use InSAR measurements of the coseismic deformation to better define the earthquake source parameters.

## 3. InSAR analysis

Immediately after the occurrence of the earthquake Frontera et al. (2012) made a DInSAR measurement of the coseismic deformation using a pair of TerraSAR-X images, and a theoretical simple numerical model based on estimated seismic rupture dislocation. They found 3 cm of vertical deformation in the northern wall of the AMF. In this chapter we present a complete InSAR analysis considering uniform and distribute slip modeling in order to understand the coseismic deformation induced by the earthquake in the frame of the local tectonic structure of the Alhama de Murcia Fault.

We use 5 Envisat ASAR images from one descending track to form 4 coseismic interferograms. The image acquisition times and interferograms constructed for this study are shown in Table 1. We can recognize the coseismic signal in each interferogram, but the phase difference also contains residual orbital errors and atmospheric phase delays (Fig. 3). To reduce these artifacts and improve the signal-to-noise ratio, we correct each interferogram of an orbital ramp and a phase/elevation correlation. Then we calculate an average interferogram using the 4 corrected interferograms (e.g. Cavalie et al., 2007). See Figs. SM1 and SM2 of the supplementary material for details.

The resulting average interferogram is shown in Fig. 4. The observed displacement along the line of sight (LOS) direction (white

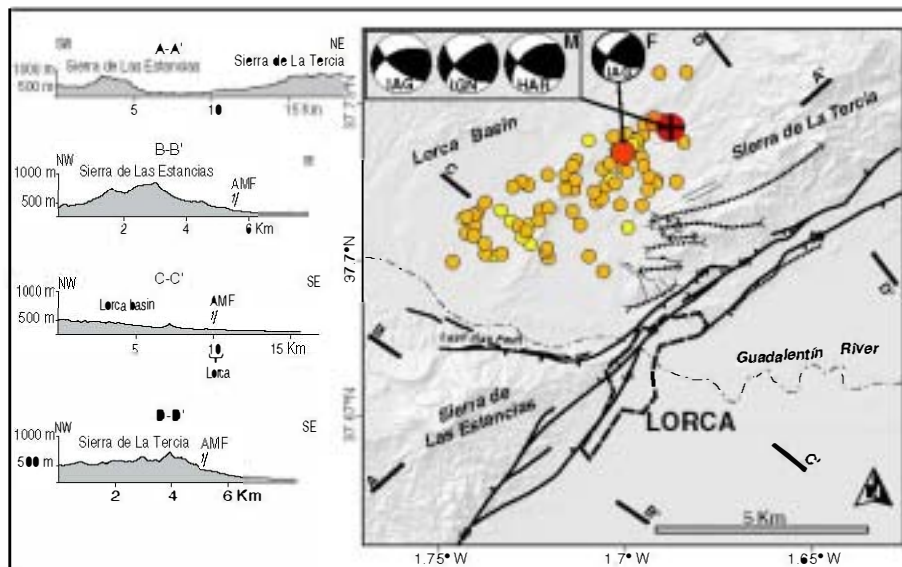


**Fig. 2.** Map of the detailed structure of the Alhama de Murcia fault in the epicentral area of the Lorca 2011 earthquake. Foreshock (F) mainshock (M) and relocated aftershocks from Lopez-Comino et al. (2012) are projected, together with the available focal solutions (see caption of Fig. 1). Mapped structures affecting the upper Miocene and Pliocene deposits are also shown: dotted lines: fold axis; continuous lines: normal faults; lines with arrows: reverse-strike slip faults. AMF (G–L): Goñar–Lorca segment; AMF (L–T): Lorca–Totana segment. To the left four transversal and longitudinal topographic profiles are shown.

**Table 1**  
Interferograms constructed for this study.

Interferograms	Date1	Date2	(*)Bperp
Int1	27-Nov-10	26-May-11	70
Int2	26-Apr-11	26-May-11	-100
Int3	26-Apr-11	25-Jun-11	80
Int4	26-Apr-11	25-Jul-11	17

(\*)Bperp: perpendicular baseline in meters.

arrow in Fig. 4) shows a region of ~5 km diameter to the NW of the AMF that moves towards the satellite (maximum of ~2 cm) and a significant larger region to the SE of the AMF that moves away from the satellite. The kind and size of the ground deformation to the north of the AMF are consistent with the coseismic deformation expected for the Mw 5.2 Lorca earthquake. Besides, roughly the same deformation is present in two independent interferograms (Fig. 3), suggesting that it is related to the same phenomena. On the other hand, the

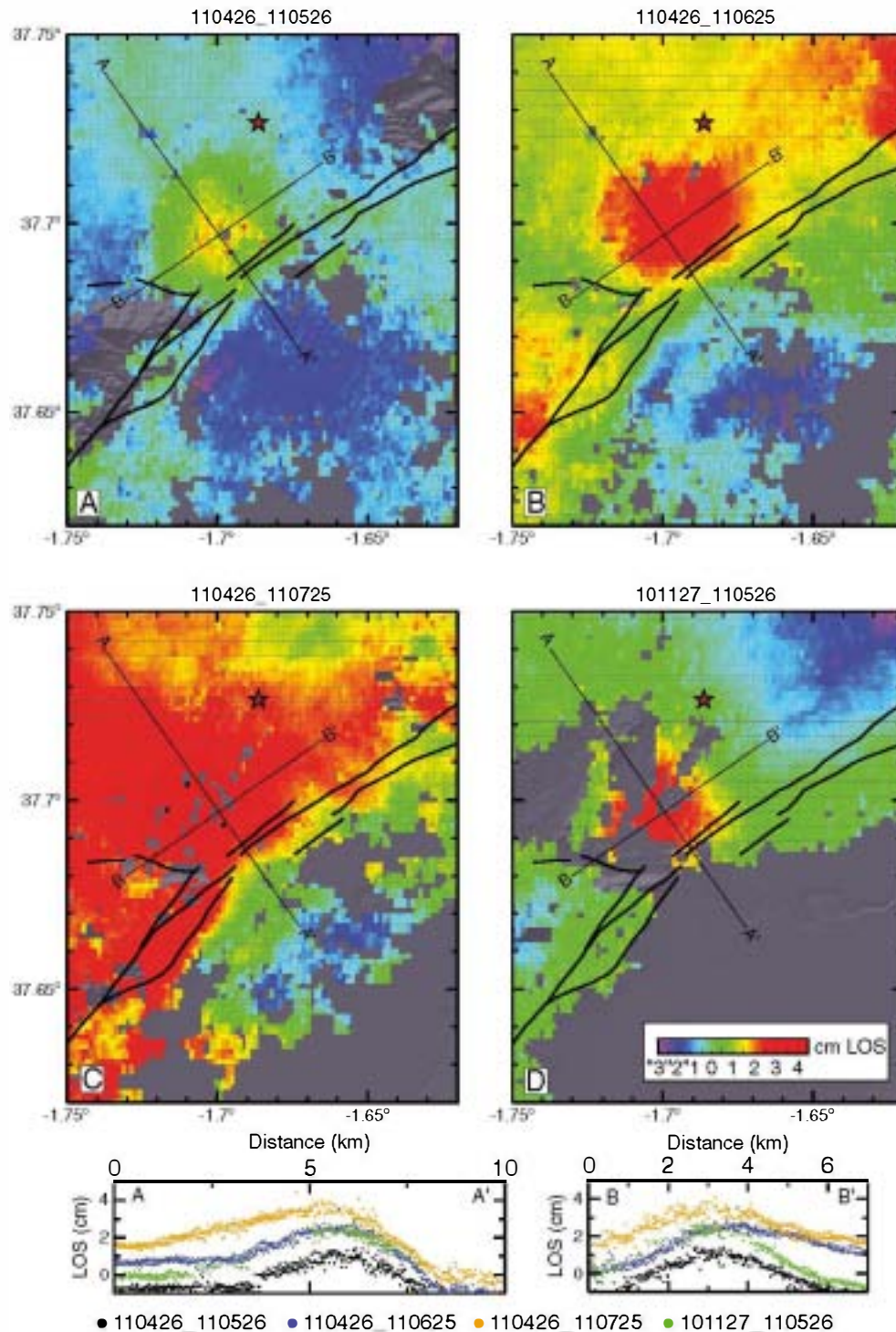


**Fig. 3.** Original coseismic interferograms used in this study. Dates of the two images combined in each case are indicated on top of each interferogram (notation yymmdd). Same color scale is used in all of them. Black lines represent tectonic structures mapped in the area. Brown star is the epicenter of the Mw 5.2 Lorca earthquake. Cross sections AA' and BB' for each interferogram are also shown. The coseismic signal can be recognized in each interferogram, but the phase difference also contains residual orbital errors and atmospheric phase delays.



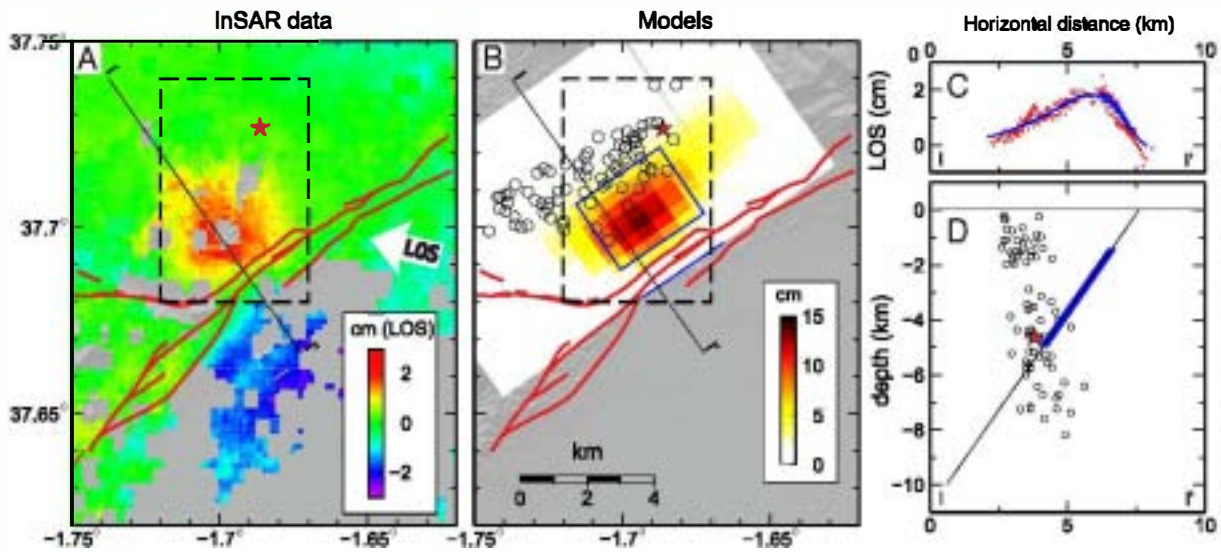


**Fig. 4.** a) Average interferogram showing surface displacement associated with the Mw 5.2 2011 Lorca earthquake. Individual interferograms were processed using the Caltech/JPL (Pasadena, CA, USA) repeat-orbit interferometry package (ROI PAC) (<http://www.roipac.org/>). The topographic phase contribution was removed using a 90 m DEM from NASA's SRTM. The orbital information used in the processing was provided by the European Space Agency (DORIS orbits). The color scale refers to change in the radar line-of-sight (LOS) direction. Positive displacements are associated with a range decrease and negative displacements are associated with a range increase (movement towards and away the satellite, respectively). The satellite to ground radar line-of-sight (LOS) is shown with a white arrow, which is inclined  $\sim 24^\circ$  from the vertical. (b) Preferred models of coseismic slip from the Lorca earthquake constrained using InSAR data. Blue rectangle represents the preferred uniform-slip model and color scale shows the preferred slip distribution model. Artifacts near the edges of the slip distribution model caused by poor resolution have been masked (see Fig. DR7 for details). (c) and (d) NW-SE cross-section perpendicular to the AMF. (c) LOS deformation observed (red points) and modeled (blue points). (d) Black line represents the fault plane used in the slip distribution inversion and thick blue line represents the fault from uniform-slip model. Red star represents the location of the mainshock and black circles represent aftershocks (Lopez-Comino et al., 2012). Black rectangle limits the region covered by data used in inversion. Red lines represent the AMF trace.

deformation to the SE of the AMF covers a much larger area than expected for a Mw 5.2 earthquake, and it is also present in non-coseismic interferograms. The amplitude of this deformation varies depending of the temporal span of the interferogram, suggesting that the phenomenon is not related to the Lorca earthquake. A previous work using InSAR temporal series recognized an important groundwater-related land subsidence in this region (Gonzalez and Fernández, 2011) during the period 1992–2007, that may be the cause of the deformation present in our interferograms SE of the AMF. Therefore, we assume that the deformation SE of the AMF is not associated with the Lorca earthquake and thus it was not considered to build coseismic models.

Note that all the interferograms include some time after the mainshock (from a minimum of 15 days in the Int1 and Int2 interferograms, to a maximum of 75 days in the Int4 interferogram, (Table 1). It is therefore possible that they include some post-seismic deformation together with the coseismic deformation.

### 3.1. Uniform-slip models

To explain the deformation pattern we model the earthquake as a dislocation in an elastic medium (Okada, 1985). We prepare InSAR data for inversion by reducing the number of points to about 1500 using a uniform sampling. Black dashed rectangle in Fig. 4 shows InSAR data used for the models (a region of  $\sim 4.5 \times 6.5$  km and a spacing of  $\sim 145$  m).

We use an inversion procedure based on a least-square minimization algorithm developed by Tarantola and Valette (1982) that assumes uniform slip on a rectangular fault plane using nine parameters (strike, dip, rake, length, bottom and top depth, average slip and geographical coordinates of the plane). Determining the nine mutually dependent parameters of the fault plane is a highly non-linear process. Besides, we only have interferograms from one satellite line-of sight direction, i.e. a single component of deformation, which provides little

constraint on the mechanism of small earthquakes (e.g. Lohman and Simons, 2005). To reduce the non-linearity we use both seismic data and a priori information on the fault geometry to constrain some of the parameters.

The strike of the fault plane is fixed at  $235^\circ$ . This value is taken from the orientation of the Alhama de Murcia Fault (AMF) at the latitude of Lorca and is consistent with published values for the strike of the focal mechanism parallel to the AMF ( $230^\circ$  from Harvard CMT solution,  $230^\circ$  from IGN solution;  $240^\circ$  from IAG solution). We fixed the rake at  $39^\circ$ , which corresponds to a sense of slip vector oriented  $196^\circ$ , consistent with published values ( $196^\circ$  from IAG solution,  $197^\circ$  from IGN solution,  $198^\circ$  from Harvard CMT solution).

We explore a series of different values for the position, dip and up-dip limit of the fault plane in 4 consecutive searches using both seismic data and a priori information on the fault geometry to constrain some of the parameters (see Fig. 5 for details). When exploring the dip we obtain a wide interval of possible values:  $55^\circ$ – $70^\circ$ , suggesting that our dataset is not very sensitive to the dip of the fault plane. We choose  $55^\circ$  because it is consistent with dip values for the fault plane parallel to the AMF from Harvard CMT solution and IAG solution ( $52^\circ$  and  $54^\circ$  respectively). Moreover the  $55^\circ$  dip is consistent with the location of the mainshock and aftershocks (Fig. 4D). Preferred values for each parameters and their standard deviation are shown in Table 2. The histograms shown in Fig. 5 reveal the estimated uncertainties for each explored parameter. The preferred uniform-slip fault plane is represented in Fig. 4B and D (blue rectangle and blue line, respectively).

Our preferred model fits well with the observed deformation pattern. However, according to our model, the hypocenter of the mainshock is out of the rupture plane (Fig. 4D). We performed models where spatial slip variations along the rupture plane are allowed to check if InSAR data are compatible with some significant slip occurring in the hypocentral area.

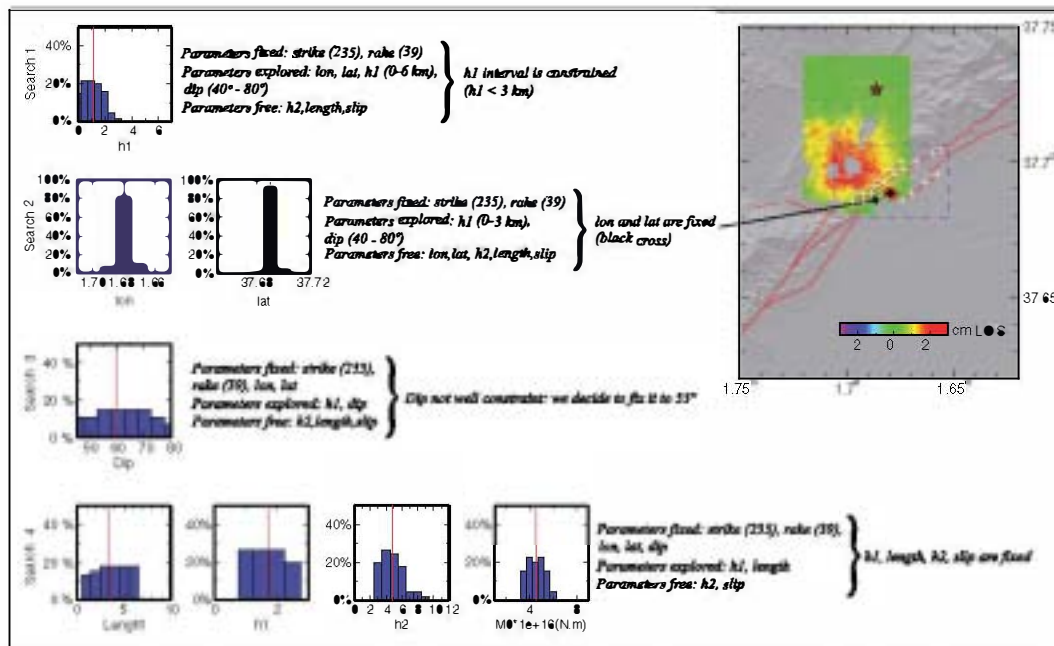


**Fig. 5.** Schematic diagram illustrating the exploration of the fault plane geometry. We explore the parameters of the fault plane in 4 consecutive searches using both seismic data and a priori information on the fault geometry to constrain some of the parameters. In each search, parameters fixed, explored and free during the inversion procedure are indicated. On the right, we indicate the output of each exploration. On the left, histograms to depict the distribution of the model parameters fixed or constrained in the explorations are shown. The map at the top right shows the explored values of longitude and latitude (Lon and Lat, which refer to the location of the center of the upper part of the fault plane projected diagonally to the surface). During Search 1, only Lat and Lon positions located on the mapped fault traces are used in the models (white crosses). In the Search 2, once the  $h_1$  is constrained, Lon and Lat are inverted, to find the location of the fault plane that better fits the InSAR observations. Preferred values for Lat and Lon are outside the mapped fault traces (red circles in the map). This might suggest that the rupture plane corresponds to a branch of the fault not completely developed (and thus it does not reach the surface yet). Preferred values for each parameters and their standard deviation are shown in Table 2.

### 3.2. Distributed-slip models

We extend the previously determined fault plane along strike and down-dip and we divide it into an array of  $20 \times 20$  elements of  $\sim 0.5$  km by 0.5 km. To solve the slip distribution along these 400 patches we use a least-squares minimization with the non-negativity constraint on the slip, imposing the rake of  $39^\circ$ . To limit oscillations of the solution, we also impose some smoothing on the solution, by minimizing the second-order derivative of the fault slip (e.g.; Du et al., 1992; Harris and Segall, 1987; Simons et al., 2002). We determine the smoothing factor from a trade-off curve that balances both the model roughness and data misfit (Fig. 6). Fig. 4B shows the best coseismic slip distribution model from InSAR data inversion. This is characterized by a zone of maximum slip of about 3 km by 3 km, with a maximum value of 15 cm. This area roughly coincides with the uniform slip fault plane (blue rectangle in Fig. 4B).

The distributed-slip model suggests that  $\sim 4$  cm of slip could have occurred near the hypocenter of the mainshock. The aftershocks are concentrated in the down dip termination of the rupture, in areas that have

little or no slip during the mainshock. The fit to the InSAR observations does not improve compared to that of the uniform slip model, suggesting that the rupture is fairly regular, but the distributed-slip model provides better compliance with seismic data. The value of  $M_0$  according to this geodetic model is  $5.177E + 16$  Nm (assuming a shear modulus of 30 GPa). It is therefore compatible with the seismic moment calculated by Lopez-Comino et al. (2012).

### 4. CFS static stress transfer models

We used the equations of Okada (1992) to obtain the strain field in the vicinity of the earthquake rupture. The Okada model computes the displacement due to a rectangular dislocation on an elastic half-space. We used a young modulus of  $8 \times 10^{10}$  Pa and a Poisson ratio of 0.25, which is equivalent to a shear modulus of  $3.2 \times 10^{10}$  Pa. From this strain

**Table 2**

Source parameters for the uniform-slip fault plane. Strike, dip and rake parameters are fixed in the inversions ( $235^\circ$ ,  $55^\circ$  and  $39^\circ$  respectively). See text for details.

Parameter	Value
*Lon	$-1.6798 \pm 0.004$
*Lat	$37.6884 \pm 0.003$
Depth to top (km)	$1.5 \pm 0.5$
Depth to bottom (km)	$4.9 \pm 1.5$
Fault length (km)	$3 \pm 1.7$
Moment (N.m)	$4.396E + 16 \pm 7.0E + 15$

\*Lon and Lat are in geographical coordinates and refers to the location of the center of the upper part of the fault plane projected diagonally to the surface.

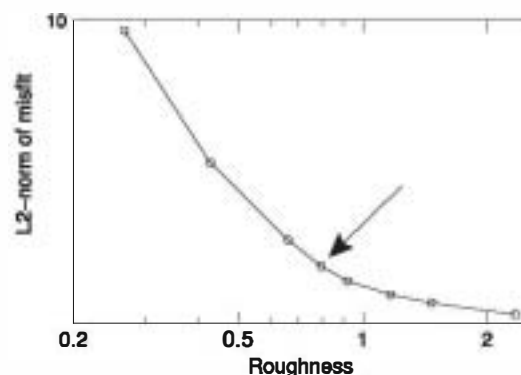


**Fig. 6.** L2 norm of least squares inversion misfit versus model roughness. Arrow indicates the location of the optimal smoothing parameter where the balance between model misfit and smoothness is achieved.



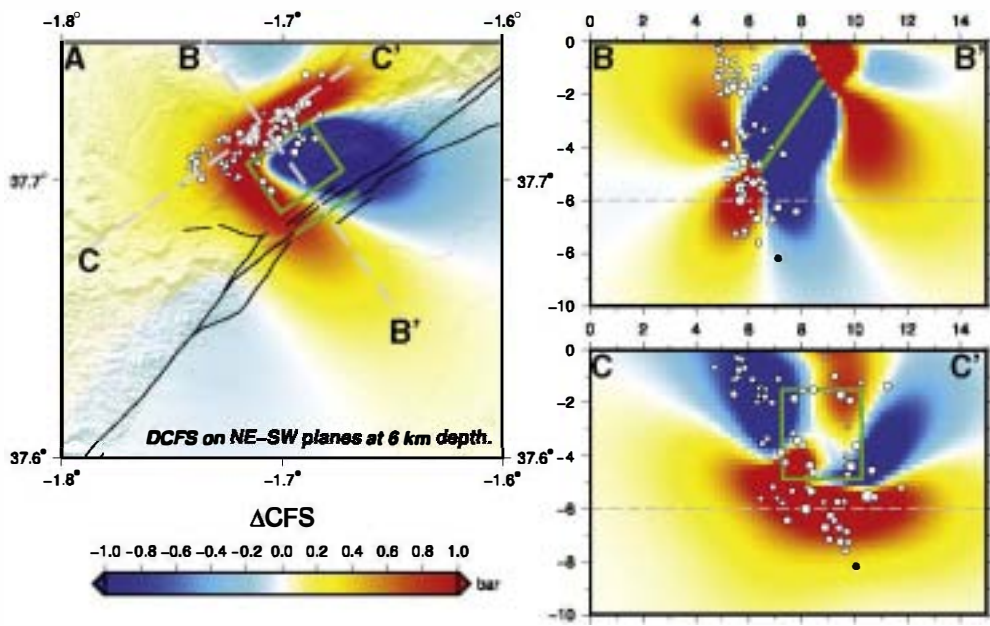


**Fig. 7.** Coulomb Failure Stress (CFS) change computed on fault planes NE-SW. A) Map of  $\Delta CFS$  at 6 km depth (shown as a dashed line in B and C); the dashed lines in A show the cross sections B-B' and C-C' (B and C subfigures respectively). The circles show the aftershocks. The rectangle shows the mainshock rupture main patch. The surface traces of the structures are shown as thin lines. Scale of B) and C) in km.

we obtain the Coulomb Failure Stress change ( $\Delta CFS$ ) defined by the equation:

$$\Delta CFS = \Delta \tau - \mu' \Delta \sigma \quad (1)$$

where  $\Delta \tau$  and  $\Delta \sigma$  are the shear and normal stress variations on the fault plane respectively, and  $\mu'$  is the apparent friction coefficient (Harris, 1998; Reasenberg and Simpson, 1992). This apparent (or effective) friction coefficient is defined as:

$$\mu' = \mu (1 - B) \quad (2)$$

where  $\mu$  is the friction coefficient and  $B$  is the Skempton coefficient which varies between 0 and 1. This coefficient introduces the role of pore pressure on the Coulomb failure function. The values of the apparent friction coefficient ranges between 0 and 0.75, being the low values commonly used for developed fault zones and higher values for less active faults (Deng and Sykes, 1997; Parsons et al., 1999;

Robinson and McGinty, 2000; Stein, 1999). The modification of this parameter influences the amount of stress change due to the normal stress variation as it can be seen from Eq. (1). A variation between 0.3 and 0.6 does not produce significant changes on the results, except for a slight modification on the off-fault lobes of the stress change.

The convenience of using a constant apparent friction coefficient is usually discussed and seems reasonable for fault zones that show a different hydraulic behavior compared to the host rock (Beeler et al., 2000), due to the high anisotropy in the damage zone (Cocco and Rice, 2002). In undrained situation during the short term post-seismic response, pore pressure changes are proportional to normal stress changes on the fault. Hence, the pore pressure variation can be included in the right term in Eq. (1) by means of Eq. (2).

We calculate static stress changes at 6 km depth on planes with the same orientation as the rupture (Fig. 7A-C), which represents the most common family of faults in the area, to study its influence on the neighboring segments. We also compute the stress change on optimally oriented faults at 2 km depth (Fig. 8) in order to study

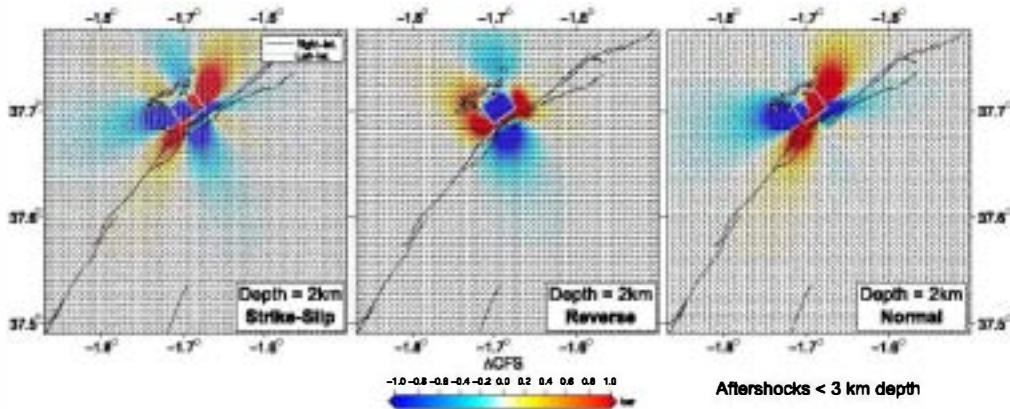


**Fig. 8.** Coulomb Failure Stress change at 2 km depth for optimally oriented A) strike slip faults, B) thrust faults and C) normal faults. The regional stress tensor is considered to have the main horizontal stress oriented NW-SE. The 2 km depth is selected in order to show the stress changes on the area where the main off-fault aftershock cluster took place. The circles show the aftershocks with hypocentral depths shallower than 3 km. The rectangle shows the projection of the main patch of the mainshock rupture. The surface traces of the structures are shown as thin lines.

the distribution of a cluster of shallow off-fault aftershocks. The positive values for  $\Delta CFS$  are interpreted as promoting the faulting, while negative values inhibit the activity.

About 75% of aftershocks accumulate mainly in the lower edge of the rupture, presenting a good correlation with positive stress change (Fig. 7). An exception to this rule is a cluster of aftershocks between 0 and 2 km deep (representing about 20% of the events). These aftershocks appear to be associated with secondary fractures, not with the rupture fault plane, and maybe generated by a family of fractures with different orientations. Models calculated on optimally oriented faults (Fig. 8) show that reverse faults oriented NE–SW receive the highest stress loading in the area where shallow off fault aftershocks accumulate. This family of reverse faults has been mapped in the zone accompanied by folding (Figs. 2 and 9) and could be the origin of this cluster of aftershocks.

With respect to the influence of the Lorca earthquake in the stress state of the surrounding segments of the AMF, our models indicate that the Goñar–Lorca segment is charged at the northern tip, and the Lorca–Totana segment is charged at the southern tip. The stress change on these segments exceeds 1 bar, a value that was shown to be sufficient for the generation of earthquake triggering (Chen et al.,

2010; Stein, 1999). The slip rate of the AMF has been calculated in previous works from neotectonic and paleoseismic records with a value ranging between 0.1 and 0.6 mm/year (Martínez-Díaz et al., 2010). The time of occurrence of an earthquake on a fault segment undergoing tectonic loading is controlled both by the stress and frictional properties on that fault and by earthquakes on other faults or segments nearby (Stein, 1999). For a fault loaded at a constant background rate, a positive change of Coulomb failure stress produces a time shift (advance) in the seismic cycle equivalent to:

$$\Delta T = \Delta CFS / \tau, \quad (3)$$

where  $\Delta T$  is the time shift,  $\Delta CFS$  is the Coulomb failure stress change and  $\tau$  is the long term stressing rate on the fault. We model the long term stressing rate on the brittle part of the fault assuming a constant displacement on the ductile deep segment of the fault (Stein et al., 1997; Toda et al., 1998). We obtain stress changes between 0.001 and 0.005 bar/year. A stress change of 1 bar represents a seismic cycle advance (time shift) equivalent to 200 to 1000 years of tectonic loading.

## 5. Discussion and conclusions

The proposed source model of the Lorca earthquake suggests that this event ruptured an area of ~4 by 3 km within a compressional strike slip duplex structure that limits the Goñar–Lorca and Lorca–Totana segments of the AMF (Figs. 2 and 9). The earthquake nucleated to the north of this structure but most of the slip concentrates on a small area located to the SW of the hypocenter coinciding with the position of the duplex in the AMF (Fig. 9). This structure could act as an asperity during the rupture. Our results show a good agreement with the main, foreshock and aftershock relocations obtained by López-Comino et al. (2012). The lateral position of maximum slip is coherent with the existence of an asymmetric bilateral rupture with 70% of the rupture propagating in SW direction described by these authors.

Our Coulomb failure stress transfer models suggest that the 2011 Lorca earthquake induced static stress loading on the adjacent segments higher than 1 bar. This represents a seismic cycle advance equivalent to 200 to 1000 years of tectonic loading. This time shift could be significant in seismic hazard assessments and should be taken into account in future studies focused on this region.

Mapped tectonic structures in the epicentral region reveal the structural complexity of this intersegment zone, where the clear and well-defined trace of the Alhama de Murcia Fault in the adjacent segments loses continuity and is characterized by several structures with different dip and orientation. The junction of structures with different orientation results in kinematically complex areas (e.g. minor structures in Fig. 2) inducing regions of distributed deformation (process zone) (Deves et al., 2011; King, 1986; King and Nabelek, 1985). This complex structural configuration is unfavorable for the occurrence of large earthquakes, but favors the occurrence of small earthquakes, like the Lorca earthquake and its aftershocks. Interestingly, the topography near the fault shows a significant change near the intersegment zone (Fig. 2): both the Goñar–Lorca and Lorca–Totana segments present a significant positive relief to the NW (Las Estancias Range and La Tercia Range) associated with the inverse component of the strain accommodated in these faults. On the other hand the intersegment zone presents a depressed region to the NW, suggesting a different way of long-term strain accommodation in this region.

From our results, we propose a hypothesis for the long-term seismic activity of the Lorca intersegment zone according to which this section of the AMF presents a characteristic seismic behavior driving faulting and rupture styles that are different from those observed in the adjacent segments (Goñar–Lorca and Lorca–Totana). Deformation is accommodated in these longer segments by localized slip in the

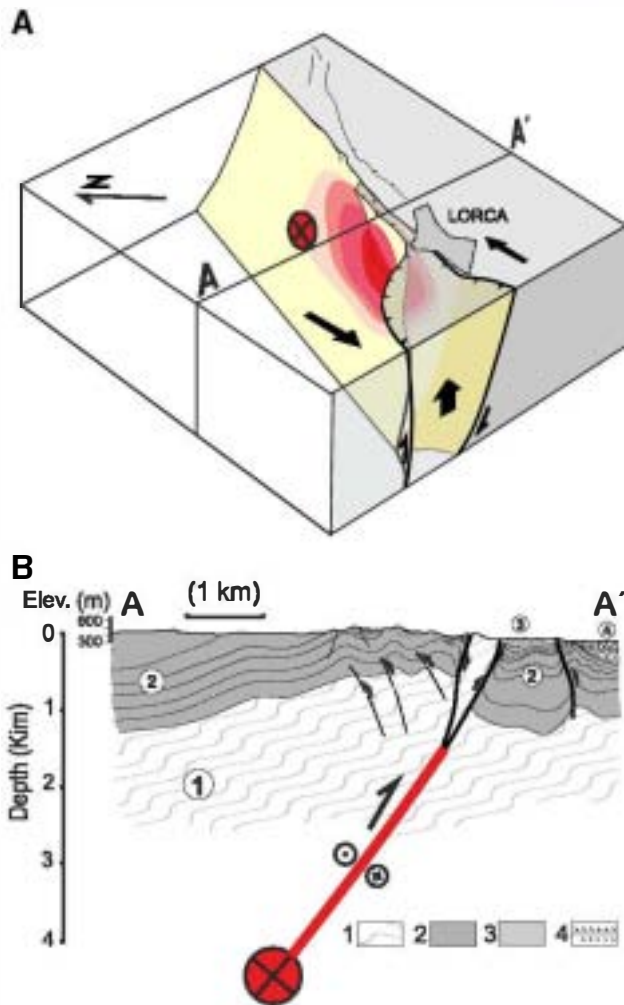


**Fig. 9.** A) Interpretative block diagram, showing the position of the inferred fault rupture in relation to the AMF structure. Most of the Mo is released to the SW of the hypocenter (circle) coinciding with the position a complexity of the fault and the area of higher deformation. B) Geological cross section through the maximum deformation area identified in the INSAR analysis. Thick line represents the estimated position of the rupture plane. Thicker segment of this line indicates the area where most of the slip concentrates (asperity). Crossed circle is the hypocenter of the Mainshock. Materials: 1: basement rocks; 2: middle–upper Miocene to Pliocene deposits; 3: older Quaternary deposits; 4: younger Quaternary (Late Pleistocene–Holocene) alluvial fans.



well-defined AMF and it builds the relief to the NW of the fault in the long-term. In the intersegment zone, deformation is accommodated in a distributed way, by slip of several structures with different orientations (sources of small earthquakes, like Lorca and its aftershocks), preventing the building of relief. The Lorca intersegment region could act as a barrier for small-moderate earthquakes ( $M_w < 7$ ), but less frequent and larger earthquakes ( $M_w > 7$ ) would be capable of propagating through the intersegment zone and rupturing both segments, as shown by available paleoseismic data (Masana et al., 2004; Ortuño et al., 2012).

In any case, the rupture process during the Lorca earthquake involved rupture directivity and heterogeneity in the slip distribution. High heterogeneity plays an important role in earthquake rupture propagation. Stored stress, strength, and frictional properties on the fault plane promote complexity in rupture processes (e.g. Page et al., 2005). The complex tectonic structure of the Lorca intersegment area favors heterogeneous slip distributions and fluctuations in rupture velocity; both may contribute to damaging high frequency ground motion (Boore and Joyner, 1978; Dunham et al., 2011; Madariaga, 1977), as occurred in the Lorca earthquake.

More paleoseismic data along the AMF, specifically in the intersegment section of the fault, and tectonic geomorphology modeling are needed to investigate this hypothesis and to answer some arising questions: can we consider the  $M_w$  5.2 Lorca earthquake as the characteristic earthquake for this area? Which is the behavior of the intersegment region during large earthquakes that rupture both segments? Can we expect peak slip at the intersegment zone as it has been suggested for some other earthquakes (e.g. the 2008  $M_w$  7.9 Wenchuan earthquake, Shen et al., 2009)? Or minimum local slip, as suggested in other cases (e.g. the 2001  $M_w$  7.8 Kokoxili earthquake, Klinger et al., 2005)? All these questions are of great importance for seismic hazard assessment in the city of Lorca.

Supplementary data related to this article can be found online at <http://dx.doi.org/10.1016/j.tecto.2012.04.010>.

## Acknowledgments

This research project was funded by Universidad Complutense de Madrid project TECIACI GR35/10-A-910368. We received financial support through Spanish projects CGL2008-01830, GEOTACTICA; CGL2009-14405-C0202-BTE; Consolider CSD2006-00041 — Topolberia and by the Junta de Andalucía project P09-RNM-5100, EC FP7 DORIS project (contract no. 242212) and finally we thank the European Space Agency (ESA) for providing the ENVISAT images (Category1-9044 project). We utilized Coulomb 3 from the USGS to model Coulomb stress changes. We thank Dr. Sylvain Barbot and Dr. Zheng-Kang Shen for their careful revisions of the manuscript and for their contributions to improve this work.

## References

Aochi, H., Fukuyama, E., Matsumura, M., 2000. Spontaneous rupture propagation on a non-planar fault in 3-D elastic medium. *Pure and Applied Geophysics* 157, 2003–2027.

Beeler, N.M., Simpson, R.W., Hickman, S.H., Lockner, D.A., 2000. Pore fluid pressure, apparent friction, and Coulomb failure. *Journal of Geophysical Research* 105 (B11), 25,533–25,542. <http://dx.doi.org/10.1029/2000JB900119>.

Boore, D.M., Joyner, W.B., 1978. The influence of rupture in coherence on seismic directivity. *Bulletin of the Seismological Society of America* 68, 283–300.

Cavalié, O., Doin, M.P., Lasserre, C., Briole, P., 2007. Ground motion measurement in the lake Mead area (Nevada, USA), by differential synthetic aperture radar interferometry time series analysis: probing the lithosphere rheological structure. *Journal of Geophysical Research* 112, B03403. <http://dx.doi.org/10.1029/2006JB004344>.

Chen, K.H., Bürgmann, R., Nadeau, R.M., 2010. Triggering effect of  $M_4$ –5 earthquakes on the earthquake cycle of repeating events at Parkfield, California. *Bulletin of the Seismological Society of America* 100 (2), <http://dx.doi.org/10.1785/0120080369>.

Cocco, M., Rice, J.R., 2002. Pore pressure and poroelasticity effects in Coulomb stress analysis of earthquake interactions. *Journal of Geophysical Research* 107 (B2), 2030 AGU.

Das, S., Aki, K., 1977. A numerical study of two-dimensional spontaneous rupture propagation. *Geophysical Journal of the Royal Astronomical Society* 50, 643–668.

Deng, J., Sykes, L.R., 1997. Stress evolution in Southern California and triggering of moderate-, small-, and micro-sized earthquakes. *Journal of Geophysical Research* 102, 411–435.

DePolo, C.M., Clark, D.G., Slemmons, D.B., Aymand, W.H., 1989. Historical Basin and Range Province surface faulting and fault segmentation. In: Schwartz, D.P., Sibson, R.H. (Eds.), *Fault Segmentation and Controls of Rupture Initiation and Termination*. U. S. Geol. Surv. Open File Rep., 89–315, pp. 131–162.

DePolo, C.M., Clark, D.G., Slemmons, D.B., Ramelli, A.R., 1991. Historical surface faulting in the Basin and Range Province, western North America—implications for fault segmentation. *Journal of Structural Geology* 13, 123–136.

Deves, M., King, G.C.P., Klinger, Y., Agnon, A., 2011. Localised and distributed deformation in the lithosphere: modelling the Dead Sea region in 3 dimensions. *Earth and Planetary Science Letters* 308, 172–184. <http://dx.doi.org/10.1016/j.epsl.2011.05.044>.

Doin, M.P., Lasserre, C., Peltzer, G., Dobre, C., 2009. Corrections of stratified tropospheric delays in SAR interferometry: validation with global atmospheric models. *Journal of Applied Geophysics* 69, 35–50. <http://dx.doi.org/10.1016/j.jappgeo.2009.03.010>.

Du, Y., Aydin, A., Segall, P., 1992. Comparison of various inversion techniques as applied to the determination of a geophysical deformation model for the 1983 Borah Peak earthquake. *Bulletin of the Seismological Society of America* 82, 1840–1866.

Dunham, E.M., Belanger, D., Cong, L., Kozdon, J.E., 2011. Earthquake ruptures with strongly rate-weakening friction and off-fault plasticity, part 2: nonplanar faults. *Bulletin of the Seismological Society of America* 101, 2308–2322.

Elliott, J.R., Parsons, B., Jackson, J.A., Shan, X., Sloan, R.A., Walker, R.T., 2011. Depth segmentation of the seismogenic continental crust: the 2008 and 2009 Qaidam earthquakes. *Geophysical Research Letters* 38, L06305. <http://dx.doi.org/10.1029/2011GL046897>.

Elliott, J.R., Nissen, E.K., England, P.C., Jackson, J.A., Lamb, S., Li, Z., Oehlers, M., Parsons, B., 2012. Slip in the 2010–2011 Canterbury Earthquakes, New Zealand. *Journal of Geophysical Research* <http://dx.doi.org/10.1029/2011JB008868>.

Fliss, S., Bhat, H.S., Dmowska, R., Rice, J.R., 2005. Fault branching and rupture directivity. *Journal of Geophysical Research* 110, B06312. <http://dx.doi.org/10.1029/2004JB003368>.

Frontera, T., Concha, A., Blanco, P., Echeverría, A., Goula, X., Arbiol, R., Khazaradze, G., Perez, F., Suriñach, E., 2012. DInSAR coseismic deformation of the May 2011  $M_w$  5.2 Lorca earthquake, (Southern Spain). *Solid Earth Discussion* 3, 111–119. <http://dx.doi.org/10.5194/se-3-111-2012>.

Gonzalez, P.J., Fernández, J., 2011. Drought-driven transient aquifer compaction imaged using multitemporal satellite radar interferometry. *Geology* 39, 551–554. <http://dx.doi.org/10.1130/G31900.1>.

Harris, R.A., 1998. Introduction to special section: stress triggers, stress shadows, and implications for seismic hazard. *Journal of Geophysical Research* 103 (B10), 24347–24358.

Harris, R.A., Day, S.M., 1993. Dynamics of fault interaction: parallel strike-slip faults. *Journal of Geophysical Research* 98, 4461–4472.

Harris, R.A., Segall, P., 1987. Detection of a locked zone at depth on the Parkfield, California, segment of the San Andreas fault. *Journal of Geophysical Research* 92, 7945–7962.

Instituto Andaluz de Geofísica (IAG), 2011. Terremoto Lorca (11 Mayo 2011). Estudios preliminares. Granada, Spain. Available at <http://www.ugr.es/iag>.

Instituto Geográfico Nacional (IGN), 2011. Serie terremoto NE Lorca (Murcia), Madrid. Available at <http://www.ign.es>.

Instituto Geológico y Minero de España (IGME), 2011. Informe Geológico Preliminar del Terremoto de Lorca del 11 de Mayo del año 2011, 5.1 Mw, Madrid. Available at <http://www.igme.es>.

Jackson, J., Bouchon, M., Fielding, E., Funning, G., Ghorashi, M., Hatzfeld, D., Nazari, H., Parsons, B., Priestley, K., Talebian, M., Tatar, M., Walker, R., Wright, T., 2006. Seismotectonic, rupture process, and earthquake-hazard aspects of the 2003 December 26 Bam, Iran, earthquake. *Geophysical Journal International* 166, 1270–1292.

King, G.C.P., 1986. Speculations on the geometry of the initiation and termination processes of earthquake rupture and its relation to morphology and geological structure. *Pure and Applied Geophysics* 124, 567–585.

King, G.C., Nabelek, J., 1985. The role of fault bends in faults in the initiation and termination of earthquake rupture. *Science* 283, 984–987.

Klinger, Y., 2010. Relation between continental strike-slip earthquake segmentation and thickness of the crust. *Journal of Geophysical Research* 115, B07306. <http://dx.doi.org/10.1029/2009JB006550>.

Klinger, Y., Xiwei, Xu, Taponnier, P., Van der Woerd, J., Lasserre, C., King, G., 2005. High-resolution satellite imagery mapping of the surface rupture and slip distribution of the  $M_w$  7.8, November 14, 2001, Kokoxili earthquake (Kunlun fault, northern Tibet, China). *Bulletin of the Seismological Society of America* 95, 1970–1987.

Li, Z., Elliott, J.R., Feng, W., Jackson, J.A., Parsons, B., Walters, R., 2011. The 2010  $M_w$  6.8 Yushu (Qinghai, China) Earthquake: constraints provided by InSAR & Body Wave Seismology. *Journal of Geophysical Research* 116, <http://dx.doi.org/10.1029/2011JB008358> 16 pp.

Lohman, R.B., Simons, M., 2005. Some thoughts on the use of InSAR data to constrain models of surface deformation: noise structure and data down sampling. *Geochimistry, Geophysics, Geosystems* 6, Q01007. <http://dx.doi.org/10.1029/2004GC000841>.

Lopez-Comino, J.A., Mancilla, F., Morales, J., Stich, D., 2012. Rupture directivity of the 2011,  $M_w$  5.2 Lorca earthquake (Spain). *Geophysical Research Letters* 39, L03301. <http://dx.doi.org/10.1029/2011GL050498>.

Loz, J.C., Oglesby, D.D., Duan, B., Wenousky, S.G., 2011. The effects of double fault bends on rupture propagation: a geometrical parameter study. *Bulletin of the Seismological Society of America* 101, 385–398.

Madariaga, R., 1977. High-frequency radiation from crack (stress drop) models of earthquake faulting. *Geophysical Journal of the Royal Astronomical Society* 51, 625–651.

- Martínez-Díaz, J.J., 2002. Stress field variety related to fault interaction in a reverse oblique-slip fault: the Alhama de Murcia Fault, Betic Cordillera, Spain. *Tectonophysics* 356, 291–305.
- Martínez-Díaz, J.J., Masana, E., Hernández-Enrile, J.L., Santanach, P., 2001. Evidence for coseismic events of recurrent prehistoric deformation along the Alhama de Murcia fault, southeastern Spain. *Geologica Acta* 36, 315–327.
- Martínez-Díaz, J.J., Masana, E., Ortuño, M., 2010. Implications of the structure of the Alhama de Murcia Fault on its paleoseismological analysis. In: Insua, J.M., Martín-González, F. (Eds.), *Contribucion de la Geología al Analisis de la Peligrosidad Sísmica, Sigüenza* (Guadalajara, Spain), pp. 97–100.
- Masana, E., Martínez-Díaz, J.J., Santanach, P., Hernández-Enrile, J.L., 2004. The Alhama de Murcia Fault (SE Spain), a seismotectonic fault in a diffuse plate boundary. *Seismotectonic implications for the Iberomagrebien region*. *Journal of Geophysical Research* 109, B01301, <http://dx.doi.org/10.1029/2002JB002359>.
- Masana, E., Pallas, R., Perea, H., Ortuño, M., Martínez-Díaz, J.J., García-Meléndez, E., Santanach, P., 2005. Large Holocene morphogenic earthquakes along the Albox fault, Betic Cordillera, Spain. *Journal of Geodynamics* 40, 119–133.
- Nissen, E., Yamini-Fard, F., Tatar, M., Gholamzadeh, A., Bergman, E., Elliott, J.R., Jackson, J.A., Parsons, B., 2010. The vertical separation of mainshock rupture and microseismicity at Qeshm Island in the Zagros fold-and-thrust belt, Iran. *Earth and Planetary Science Letters* 296, 181–194, <http://dx.doi.org/10.1016/j.epsl.2010.04.049>.
- Okada, Y., 1985. Surface deformation to shear and tensile faults in a half space. *Bulletin of the Seismological Society of America* 75, 1135–1154.
- Okada, Y., 1992. Internal deformation due to shear and tensile faults in a half-space. *Bulletin of the Seismological Society of America* 82, 1018–1040.
- Ortuño, M., Masana, E., García Meléndez, E., Martínez-Díaz, J., Štěpančíková, P., Cunha, P.P., Sobhbat, R., Canora, C., Buylaert, J.P., Murria, A.S., 2012. An exceptionally long paleoseismic record of a slow-moving fault: the Alhama de Murcia fault (Eastern Betic Shear Zone, Spain). *Bulletin of the Geological Society of America*. doi:10.1130/B30558.1.
- Page, M.T., Dunham, E.M., Carlson, J.M., 2005. Distinguishing barriers and asperities in near-source ground motion. *Journal of Geophysical Research* 110, B11302, <http://dx.doi.org/10.1029/2005JB003736>.
- Parsons, T., Stein, R.S., Simpson, R.W., Reasenberg, P.A., 1999. Stress sensitivity of fault seismicity: a comparison between limited-offset oblique and major strike-slip faults. *Journal of Geophysical Research* 104 (B9), 20183–20202.
- Reasenberg, P.A., Simpson, R.W., 1992. Response of regional seismicity to the static stress change produced by the Loma Prieta earthquake. *Science* 255, 1687–1690.
- Robinson, R., McGinty, P.J., 2000. The enigma of the Arthur's Pass, New Zealand, earthquake 2. The aftershock distribution and its relation to regional and induced stress fields. *Journal of Geophysical Research* 105 (B7), 16139–16150.
- Scholz, C.H., 1990. *Mechanics of Earthquakes and Faulting*. Cambridge University Press. 461pp.
- Shen, Z.-K., Sun, J., Zhang, P., Wan, Y., Wang, M., Bürgmann, R., Zeng, Y., Gan, W., Liao, H., Wang, Q., 2009. Slip maxima at fault junctions and rupturing of barriers during the 2008 Wenchuan earthquake. *Nature Geoscience* 2, 718–724, <http://dx.doi.org/10.1038/ngeo636>.
- Shengji, W., Fielding, E., Leprince, S., Sladen, A., Avouac, J.P., Helmberger, D., Hauksson, E., Chu, R., Simons, M., Hudnut, K., Herring, T., Briggs, R., 2011. Superficial simplicity of the 2010 El Mayor-Cucapah earthquake of Baja California in Mexico. *Nature Geoscience* 4, 615–618.
- Silva, P.G., Goy, J.L., Somoza, L., Zazo, C., Bardaji, T., 1993. Landscape response to strike-slip faulting linked to collisional settings: quaternary tectonics and basin formation in the Eastern Betics, Southeastern Spain. *Tectonophysics* 224, 289–303.
- Simons, M., Fialko, Y., Rivera, L., 2002. Coseismic deformation from the 1999 Mw 7.1 Hector Mine, California, earthquake as inferred from InSAR and GPS observations. *Bulletin of the Seismological Society of America* 92, 1390–1402, <http://dx.doi.org/10.1785/0120000933>.
- Stein, R.S., 1999. The role of stress transfer in earthquake occurrence. *Nature* 402, 605–609.
- Stein, R.S., Barka, A.A., Dieterich, J.H., 1997. Progressive failure on the North Anatolian fault since 1939 by earthquake stress triggering. *Geophysical Journal International* 128, 594–604.
- Tarantola, A., Valette, B., 1982. Generalized nonlinear inverse problem solved using the least squares criterion. *Reviews of Geophysics* 20, 219–232.
- Toda, S., Stein, R.S., Reasenberg, P.A., Dieterich, J.H., Yoshida, A., 1998. Stress transferred by the 1995 Mw = 6.9 Kobe, Japan, shock: effect on aftershocks and future earthquake probabilities. *Journal of Geophysical Research* 103 (B10), 24543–24565.
- Visser, R.L.M., Meijninger, B.M.L., 2011. The 11 May 2011 earthquake at Lorca (SE Spain) viewed in a structural-tectonic context. *Solid Earth Discussion* 3, 527–540.
- Wesnousky, S., 2006. Predicting the end points of earthquake ruptures. *Nature* 444, <http://dx.doi.org/10.1038/nature05275>.
- Zebker, H., Rosen, P., Goldstein, R.M., 1994. On the derivation of coseismic displacement fields using differential radar interferometry: the Landers earthquake. *Journal of Geophysical Research* 99, 19 617–19 634.

## REFERENCES CITED IN SUPPLEMENTARY DATA

- Doin, M.P., Lasserre, C., Peltzer, G., Doubre, C., 2009b. Corrections of stratified tropospheric delays in SAR interferometry: validation with global atmospheric models. *Journal of Applied Geophysics* 69, 35–50, <http://dx.doi.org/10.1016/j.jappgeo.2009.03.010>.
- Cavalié, O., Doin, M.P., Lasserre, C., Briole, P., 2007b. Ground motion measurement in the lake Mead area (Nevada, USA), by differential synthetic aperture radar interferometry time series analysis: probing the lithosphere rheological structure. *Journal of Geophysical Research* 112, B03403, <http://dx.doi.org/10.1029/2006JB004344>.
- Zebker, H., Rosen, P., Goldstein, R.M., 1994b. On the derivation of coseismic displacement fields using differential radar interferometry: the Landers earthquake. *Journal of Geophysical Research* 99, 19 617–19 634.